

# Learning in Sinusoidal Spaces with Physics-Informed Neural Networks

Jian Cheng Wong, Chinchun Ooi, Abhishek Gupta, and Yew-Soon Ong, *Fellow, IEEE*

**Abstract**— A physics-informed neural network (PINN) uses physics-augmented loss functions, e.g., incorporating the residual term from governing differential equations, to ensure its output is consistent with fundamental physics laws. However, it turns out to be difficult to train an accurate PINN model for many problems in practice. In this paper, we address this issue through a novel perspective on the merits of learning in sinusoidal spaces with PINNs. By analyzing asymptotic behavior at model initialization, we first prove that a PINN of increasing size (i.e., width and depth) induces a bias towards *flat* outputs. Notably, a flat function is a *trivial* solution to many physics differential equations—hence, deceptively minimizing the residual term of the augmented loss while being far from the true solution. We then show that the sinusoidal mapping of inputs—in an architecture we label as *sf-PINN*—is able to elevate output variability, thus avoiding being trapped in the deceptive local minimum. In addition, the level of variability can be effectively modulated to match high-frequency patterns in the problem at hand. A key facet of this paper is the comprehensive empirical study that demonstrates the efficacy of learning in sinusoidal spaces with PINNs for a wide range of forward and inverse modelling problems spanning multiple physics domains.

**Index Terms**—Differential equations, physics-informed neural networks, sinusoidal spaces.

## I. INTRODUCTION

THEORY-GUIDED machine learning has been drawing increasing interest in recent years [1, 2]. Physics-informed neural networks—PINNs as per Raissi *et al.* [3]—in particular have leveraged the expressiveness of deep neural networks (DNNs) to model the dynamical evolution  $\hat{u}(x, t; \mathbf{w})$  of physical systems in space  $x \in \Omega$  and time  $t \in [0, T]$ , via the optimization of network parameters  $\mathbf{w}$ . In many of these physical systems,  $u$  can be mathematically described by a known prior derived from the underlying physics, such as governing equations in the form of ordinary differential equations (ODEs) or partial differential equations (PDEs). The uniqueness of a PINN lies in incorporating the residual term for such differential equations into the training loss function. This

Jian Cheng Wong is with the Institute of High Performance Computing (IHPC), Agency for Science, Technology and Research (A\*STAR), Singapore, and is also with the School of Computer Science and Engineering, Nanyang Technological University (NTU), Singapore (email: [wongj@ihpc.a-star.edu.sg](mailto:wongj@ihpc.a-star.edu.sg)).

Chinchun Ooi is with the Institute of High Performance Computing (IHPC), Agency for Science, Technology and Research (A\*STAR), Singapore (email: [ooicc@ihpc.a-star.edu.sg](mailto:ooicc@ihpc.a-star.edu.sg)).

physics-augmented loss thus acts as a penalty to constrain the PINN from violating the differential equations, ensuring that its output obeys underlying governing physics.

There has been a recent surge in PINN studies for various science and engineering problems, including in the fields of fluid mechanics [4, 5], solid mechanics [6, 7] and optics [8, 9]. These problems have one common characteristic: ground truth data is difficult and expensive to obtain (often requiring extensive domain expertise), whether it be through computational simulations or real-world experiments. In such settings, the imposition of physics-based constraints can reduce overfitting to sparse data by ensuring the consistency of a PINN’s outputs with fundamental physics laws. Given the resultant proficiency in learning from limited (or even *zero*) labelled data, variants of PINNs have begun to attract attention for their utility in the following three areas of application:

1. PINNs form a new class of mesh-free methods to solve differential equations, i.e., the *forward problem* [10, 11, 12, 13, 14, 15]. Essentially, the problem is transformed to one of neural network training requiring no labelled data and no explicit discretization. The loss function is simply defined by residual terms from the differential equations and prescribed initial or boundary conditions (referred to as the *physics loss*).
2. PINNs have been extended to solve *inverse problems*, i.e., inferring *unknown* physics in differential equations from limited data [16, 17, 18]. For example, they have been successfully applied to quantify fluid flows from visualization or sensor data [4], and in the design of metamaterials [8].
3. PINNs have also been used to build accurate surrogate models from sparse data by being supplemented with known physics priors [19, 20, 21, 22].

Despite the strong practical motivations in a wide range of applications, it remains difficult to train accurate PINN models. For example, in many works, training iterations for PINNs far exceed those needed for typical DNNs [23, 24] even using state-of-the-art stochastic gradient descent (SGD) methods (such as ADAM [25]). As a result, there has been significant effort of late to improve PINN trainability by balancing the different

Abhishek Gupta is with the Singapore Institute of Manufacturing Technology (SIMTech), Agency for Science, Technology and Research (A\*STAR), Singapore (email: [abhishek\\_gupta@simtech.a-star.edu.sg](mailto:abhishek_gupta@simtech.a-star.edu.sg)).

Yew-Soon Ong is Chief Artificial Intelligence Scientist with the Agency for Science, Technology and Research (A\*STAR), Singapore, and is also with the Data Science and Artificial Intelligence Research Centre, School of Computer Science and Engineering, Nanyang Technological University (NTU), Singapore (email: [aysong@ntu.edu.sg](mailto:aysong@ntu.edu.sg)).

components in its loss function [26, 27, 28, 29, 30]. However, this is a highly non-trivial task as the individual components vary greatly in magnitude and convergence rate during training.

Given the above, in this paper, we analyze the merits of learning in *sinusoidal space* for accurate PINNs. The paper contains three thematic portions. First, we theoretically examine the behavior of the outputs of a standard PINN in the asymptotic case of width and depth growing to infinity, and relate this to its trainability issue. *Going beyond the vanishing gradient problem of DNNs [31], we uncover a major reason for the difficulty in training PINNs stems from the model's strong initial bias towards flat outputs.* In practice, the outputs are flat almost everywhere under many commonly used activation functions in PINNs, such as “tanh”. This is particularly undesirable for PINNs since a flat function is a *trivial* solution to many physics differential equations. As a result, the PINN gets trapped in a deceptive local optimum (that minimizes PDE/ODE residual terms) right from the onset of training, while still being far away from the true solution that must also satisfy initial and/or boundary conditions.

Based on this revelation, a new perspective on the utility of learning in sinusoidal spaces is laid out next; in particular, how they extricate PINNs from the local optimum trap. We introduce a class of sinusoidal mappings which convert a PINN's low dimensional spatial-temporal inputs into a higher dimensional sinusoidal space. The resultant neural architecture is referred to as *sf*-PINN. We show that in practice a *sf*-PINN has input gradients with almost uniform variability across the entire input domain. Furthermore, we can modulate the initialized variability to match high-frequency patterns in the problem at hand—a distinct property absent from the standard PINN model. It is also worth noting the ubiquity of sinusoidal structures in analytical solutions of dynamical systems, such as electromagnetics, advection-diffusion equations, etc., which suggests their natural suitability for learning effective representations for PINNs.

Lastly, our comprehensive experimental study demonstrates that *sf*-PINNs are indeed able to achieve better performance (a few orders of magnitude in terms of accuracy) than standard PINNs across a wide range of forward and inverse modelling problems, spanning multiple physics domains. Interestingly, the results also suggest that *sf*-PINNs are less sensitive to the composition of the physics loss components. This makes finding the right balance for them less critical, offering an alternate path to the handling of loss components that is different from those in the literature.

The remainder of the paper is organized as follows. In Section II, we describe the standard PINN model and theoretically examine its asymptotic behavior. Section III introduces sinusoidal mappings as an approach to mitigate the theoretical limitations we uncover. Sections IV and V enumerate the extensive experimental studies conducted to illustrate the advantage of *sf*-PINNs across multiple forward and inverse modelling problems, respectively. Concluding remarks and direction for future research are then presented in Section VI.

## II. STANDARD PINNS AND THEIR LIMITATIONS

### A. Overview of PINNs

In this sub-section, we briefly outline the concept and methodology as commonly employed in current literature and software [32, 33, 34]. A typical PINN considers a fully-connected feed-forward DNN representation  $\hat{u}(x, t; \mathbf{w})$  for modelling the dynamical process  $u$  of a physical system in space  $x \in \Omega$  and time  $t \in [0, T]$  domain, with network parameters  $\mathbf{w}$  to be optimized. The spatial domain usually has 1-, 2- or 3-dimensions in physical problems. Furthermore,  $u$  can be mathematically described by known priors such as differential equations of the general form [11, 3]:

$$\mathcal{N}_t[u(x, t)] + \mathcal{N}_x[u(x, t)] = 0, \quad x \in \Omega, t \in [0, T], \quad (1)$$

$$u(x, 0) = u_o(x), \quad x \in \Omega, \quad (1b)$$

$$\mathcal{B}[u(x, t)] = g(x, t), \quad x \in \partial\Omega, t \in [0, T], \quad (1c)$$

where  $\mathcal{N}_t[\cdot]$  is the temporal derivative, and  $\mathcal{N}_x[\cdot]$  is a general nonlinear differential operator which can include any combination of non-linear terms of spatial derivatives, such as the first and second order derivatives  $u_x(x, t)$  and  $u_{xx}(x, t)$ , respectively. The initial condition at  $t=0$  is defined by  $u_o(x)$ , and the boundary operator  $\mathcal{B}[\cdot]$  enforces the desired condition  $g(x, t)$  at the domain boundary  $\partial\Omega$ . This  $\mathcal{B}[\cdot]$  can be an identity operator (Dirichlet boundary condition) or a differential operator (Neumann boundary condition).

As an example, consider the wave equation (describing phenomena such as electromagnetic propagation) which in 1D reads  $u_{tt} = c^2 u_{xx}$ , where  $\mathcal{N}_t[u] = u_{tt}$  and  $\mathcal{N}_x[u] = -c^2 u_{xx}$ . It contains a coefficient  $c$  representing the velocity of the wave. The differential equation in isolation has trivial solutions  $u(x, t) = \mu$ , where  $\mu$  is any constant, among many other solutions. A unique solution must therefore be obtained by satisfying the differential equation in combination with the initial condition (1b) and/or boundary condition (1c) as prescribed by the problem of interest.

#### 1) PINN Training Loss

The loss function of a PINN is defined as [11, 3]:

$$\mathcal{L} = \mathcal{L}_{Data} + \lambda_{DE}\mathcal{L}_{DE} + \lambda_{IC}\mathcal{L}_{IC} + \lambda_{BC}\mathcal{L}_{BC}, \quad (2)$$

which includes the data loss component (when data is available),

$$\mathcal{L}_{Data} = \frac{1}{n} \sum_{i=1}^n (u_i - \hat{u}_i)^2, \quad (2b)$$

and the physics loss components,

$$\mathcal{L}_{DE} = \|\hat{u}_t(\cdot; \mathbf{w}) + \mathcal{N}_x[\hat{u}(\cdot; \mathbf{w})]\|_{\Omega \times [0, T]}^2, \quad (2c)$$

$$\mathcal{L}_{IC} = \|\hat{u}(\cdot, 0; \mathbf{w}) - u_o\|_{\Omega}^2, \quad (2d)$$

$$\mathcal{L}_{BC} = \|\mathcal{B}[\hat{u}(\cdot; \mathbf{w})] - g(\cdot)\|_{\partial\Omega \times [0, T]}^2. \quad (2e)$$

The relative weights  $\lambda$ s in (2) control the trade-off between different components in the loss function, and need to be scaled depending on the problem at hand. The computation of the loss (2) involves matching the PINN output  $\hat{u}$  against target  $u$  over

$n$  labelled samples (2b), substitution of the output  $\hat{u}$  into the differential equation for evaluating the residuals (2c) over the input domain  $\Omega \times [0, T]$ , as well as matching the output  $\hat{u}$  against initial conditions at  $t=0$  (2d), and boundary conditions over the domain boundary  $\partial\Omega$  (2e). In solving forward problems, the data loss component  $\mathcal{L}_{Data}$  (2b) may be omitted. The physics loss component (2c-e) is defined over a continuous domain, but for practical reasons, we compute the residuals over a finite set of  $m$  collocation points  $D = \{(x_i, t_i)\}_{i=1}^m$ . These points are sampled, for example, using a uniform grid or randomized Latin hypercube sampling from the spatial-temporal domain. Differential operators, such as  $\hat{u}_t(x, t; \mathbf{w})$ ,  $\hat{u}_x(x, t; \mathbf{w})$ ,  $\hat{u}_{xx}(x, t; \mathbf{w})$ , are required for the evaluation of the residuals. For this reason, the higher order differentiable ‘‘tanh’’ activation function is most widely adopted for PINNs [11, 3, 32, 34]. The computation of differential operators can then be conveniently obtained via automatic differentiation [35].

## B. Empirical Observation of Trainability Issues

PINNs are found to be more challenging to train than usual DNNs, which has so far hindered the full potential of PINN applications. To understand some of the factors causing this phenomenon, we construct a synthetic 1D differential equation problem for observing the training behavior of PINNs. Consider the 1D multi-frequency ODE problem,

$$u_{xx} + h^2 u = (a_1 - a_1 a_2^2)h^2 \sin(a_2 h x) + (b_1 - b_1 b_2^2)h^2 \sin(b_2 h x), \quad (3)$$

which is solved with the following boundary conditions:

$$u(0) = 0, \quad (3b)$$

$$u_x(0) = h + a_1 a_2 h + b_1 b_2 h. \quad (3c)$$

The parameters in (3) are  $h=8$ ,  $a_1=1$ ,  $a_2=6$ ,  $b_1=1$ ,  $b_2=5$ .

We assume a forward problem setup, i.e., training a standard

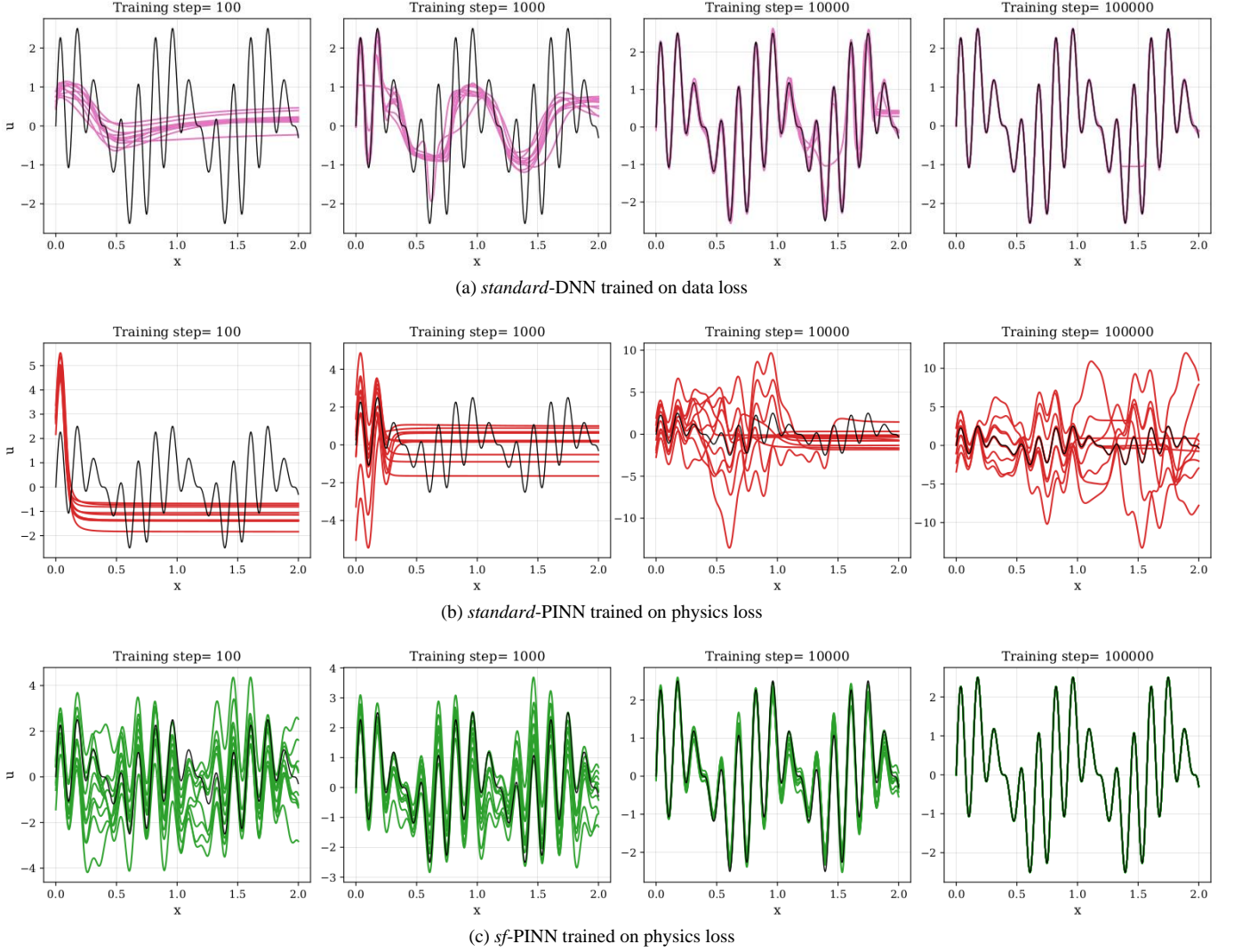


Fig. 1. The training history of (a) standard-DNN, (b) standard-PINN, and (c) sf-PINN on synthetic 1D multi-frequency ODE example. Their outputs from 10 independent runs after  $10^2, 10^3, 10^4$  and  $10^5$  optimization steps are plotted in color lines. Note that the output of the standard PINN remains mostly flat even after 1000 training steps. The ground truth solution is indicated by black line. In each optimization step, the loss function is computed from 100 randomly selected points  $x \in [0, 2]$ , plus 1 fixed boundary point ( $x=0$ ).

PINN model to solve (3) based on residuals from 10k collocation points sampled from the input domain  $x \in [0,2]$ , *without* using any labelled data. The network has 1 input node (the  $x$  coordinate), 4 hidden layers (64-20-20-20 nodes), and 1 output node ( $u$ ). Following common model configurations in the literature [3, 11, 32, 34], all hidden layers, except the final (output) layer, include a bias term and use the “tanh” activation function. The final layer uses the “linear” activation function. The network weights are initialized using Xavier initialization [36], biases are initialized to 0, and the state-of-the-art ADAM algorithm is used for training. It is recognized that the convergence of SGD, including that of ADAM, is highly sensitive to the learning rate. Hence, a popular learning plan to reduce learning rate by half on plateauing is adopted [37]. In general, this strategy tends to improve convergence. For comparison, we also train a standard DNN model with the exact same model configuration, except that it learns from labelled data sampled from the ground truth solution at the 10k collocation points.

The training behaviors based on 10 independent runs are visualized in Figure 1. The outputs from both *standard*-NN and *standard*-PINN are very flat upon initialization, and this persists even after several hundred optimization steps. For the *standard*-NN (Figure 1a), the lower frequency pattern is learned before higher frequency. This observation is consistent with theoretical analysis from prior studies [38]. We observe a different training behavior for the *standard*-PINN (Figure 1b), which follows a very different loss landscape. Much of the learning effort is devoted to striking a balance between different loss terms representing the differential equation and the boundary condition. *Importantly, the network output remains very flat across most of the input domain at initialization and even after a significant number of optimization steps.* At the end of 100k optimization steps, many PINN training runs are still trapped in bad local optima that are far away from the true solution.

### C. Theoretical Analysis of Trainability Issues

In this subsection, we explain the predisposition of a standard PINN model to produce and be trapped at flat outputs under a typical parameter initialization scheme.

The convergence of PINNs have been investigated in recent studies. Shin *et al.* [26] showed that the convergence of empirical PINN loss—i.e., (2c-e) estimated from the samples—indeed leads to the solution to the PDE (under mild assumptions). Wang *et al.* [27] studied the trainability of PINNs through the lens of the Neural Tangent Kernel (NTK), and found significant discrepancy in convergence rate of different loss components. Multiple competing loss components in PINNs can lead to local minima when optimized together [29], thus posing an optimization challenge. These studies then propose to improve the convergence by prioritizing the initial and boundary conditions (2d-e), or adaptively calibrating the composition of loss components during training, for example by annealing. The current paper offers new insights to the factors affecting the trainability of PINNs and proposes a different approach to improve model accuracy.

#### 1) Asymptotic Behavior at Initialization

Consider the result below that holds for PINN models of the type in Section II-B.

*Proposition 1.* Let  $\hat{u}(x; \mathbf{w})$  be the output of a fully connected PINN with  $l$  hidden layers,  $n$  neurons per layer, contraction mapping activation function  $f$ , i.e.,  $\|f(x) - f(x')\|_2^2 < \|x - x'\|_2^2, \forall x \neq x'$ , and parameters  $\mathbf{w}$ . Let all the dense layers be initialized by the Xavier method for network parameters, i.e., the  $w$ ’s are independently and identically (i.i.d.) sampled from Gaussian distribution  $\mathcal{N}(0, 1/n)$ . Then,  $\hat{u}(x; \mathbf{w})$  is almost surely a flat function, i.e.,  $\lim_{l, n \rightarrow \infty} \hat{u}(x; \mathbf{w}) = \mu, \forall x$ , with probability 1, at initialization.

*Proof:*

Let  $\phi_k(x_k; \mathbf{W}_k) = f(\mathbf{W}_k x_k) \in \mathbb{R}^n$  denote the output of  $k$ -th layer corresponding to input  $x_k \in \mathbb{R}^n$ , linear matrix  $\mathbf{W}_k \in \mathbb{R}^{n \times n}$  such that  $w_{i,j} \sim \mathcal{N}(0, 1/n)$ , and activation  $f$ . We first show that *an infinitely wide dense layer (before activation) is convergent with probability 1 to an isometry*, i.e.,

$$\|\mathbf{W}_k x_k - \mathbf{W}_k x'_k\|_2^2 = \|\mathbf{W}_k(x_k - x'_k)\|_2^2 \xrightarrow{P} \|x_k - x'_k\|_2^2, \quad (4)$$

for any 2 inputs  $x_k \neq x'_k$  when  $n \rightarrow \infty$ . Here,  $\|\cdot\|_2$  refers to the Euclidean norm. Let us consider an element of the linear mapping  $y_i = \sum_{j=1}^n w_{i,j}(x_k - x'_k)_j$ . It is straightforward to see that  $y_i$  is the sum of independent normally distributed random variables with  $E[y_i] = 0$ , and,

$$\text{Var}(y_i) = \text{Var}\left(\sum_{j=1}^n w_{i,j}(x_k - x'_k)_j\right) = \sum_{j=1}^n \text{Var}(w_{i,j})(x_k - x'_k)_j^2 = \frac{1}{n} \sum_{j=1}^n (x_k - x'_k)_j^2 = \frac{1}{n} \|x_k - x'_k\|_2^2. \quad (5)$$

That is,  $y_i \sim \mathcal{N}(0, \frac{1}{n} \|x_k - x'_k\|_2^2)$ . Now we make use of the fact that:

$$y_i^2 \sim \frac{1}{n} \|x_k - x'_k\|_2^2 \chi_1^2 \equiv \Gamma\left(\frac{1}{2}, \frac{2}{n} \|x_k - x'_k\|_2^2\right), \quad (6)$$

where  $\chi_1^2$  is a Chi-square distribution with 1 degree of freedom, and  $\Gamma(k, \Theta)$  is a Gamma distribution with shape and scale parameters  $k$  and  $\Theta$  respectively. Thus, the squared norm of linear mapping follows a Gamma distribution:

$$\|\mathbf{W}_k(x_k - x'_k)\|_2^2 = \sum_{i=1}^n \left( \sum_{j=1}^n w_{i,j}(x_k - x'_k)_j \right)^2 = \sum_{i=1}^n y_i^2 \sim \Gamma\left(\frac{n}{2}, \frac{2}{n} \|x_k - x'_k\|_2^2\right). \quad (7)$$

Now, we obtain the mean and variance of the Gamma distribution,

$$E[\|\mathbf{W}_k(x_k - x'_k)\|_2^2] = \frac{n}{2} \frac{2}{n} \|x_k - x'_k\|_2^2 = \|x_k - x'_k\|_2^2, \quad (8a)$$

$$\text{Var}(\|\mathbf{W}_k(x_k - x'_k)\|_2^2) = \frac{n}{2} \left( \frac{2}{n} \|x_k - x'_k\|_2^2 \right)^2 = \frac{2}{n} (\|x_k - x'_k\|_2^2)^2. \quad (8b)$$

Taking the limit  $n \rightarrow \infty$ , the variance (8b) goes to zero and the distribution converges to its mean (8a), hence (4) is proved.

With a contractive activation,

$$\forall x \neq x', \|\phi_k(x_k; \mathbf{w}_k) - \phi_k(x'_k; \mathbf{w}_k)\|_2^2 = \|f(\mathbf{W}_k x_k) - f(\mathbf{W}_k x'_k)\|_2^2 < \|x_k - x'_k\|_2^2, \text{ as } n \rightarrow \infty, \quad (9)$$

because  $\|f(\mathbf{W}_k x_k) - f(\mathbf{W}_k x'_k)\|_2^2 < \|\mathbf{W}_k x_k - \mathbf{W}_k x'_k\|_2^2$  and  $\|\mathbf{W}_k x_k - \mathbf{W}_k x'_k\|_2^2 \xrightarrow{P} \|x_k - x'_k\|_2^2$  as  $n \rightarrow \infty$ . This implies that  $\phi_k(x_k; \mathbf{w}_k)$  is asymptotically contractive.

Following (9), we define constants  $0 \leq C_k < 1$  such that  $\|\phi_k(x_k; \mathbf{w}_k) - \phi_k(x'_k; \mathbf{w}_k)\|_2^2 \leq C_k \|x_k - x'_k\|_2^2$ ,  $k = 1, \dots, l$ . Note that  $\hat{u}(x; \mathbf{w}) = \phi_l(\phi_{l-1}(\dots \phi_1(x; \mathbf{w}_1); \mathbf{w}_2) \dots; \mathbf{w}_l)$ , with the input of  $k$ -th hidden layer  $x_k$  being the output of  $(k-1)$ -th hidden layer  $\phi_{k-1}(x_{k-1}; \mathbf{w}_{k-1})$ . The resulting network output thus satisfies,

$$\forall x \neq x', \|\hat{u}(x; \mathbf{w}) - \hat{u}(x'; \mathbf{w})\|_2^2 \leq C \|x - x'\|_2^2, \quad (10)$$

with  $C = \prod_{k=1}^l C_k$ . Taking the limit  $l \rightarrow \infty$ , we get  $C \rightarrow 0$ . This result implies  $\lim_{l, n \rightarrow \infty} \hat{u}(x; \mathbf{w}) \rightarrow \mu, \forall x$  as stated in *Proposition 1*.  $\blacksquare$

*Proposition 1* suggests that a PINN with contractive activation  $f$  is asymptotically flat upon Xavier initialization. Such activation functions include “tanh” (the most widely adopted in PINNs), and other smooth monotonic activations such as “sigmoid” and “softplus” which are also used in PINNs. Note that a “relu” activation function also falls under this criteria, since the inputs to the activation have a symmetric distribution around zero upon Xavier initialization. Such asymptotic behavior with  $\hat{u}(x, t; \mathbf{w}) = \mu$  is deleterious for PINN training, because a flat function is a trivial local minimum of the loss component (2c) for many commonly encountered physics differential equations, such as the wave equation ( $u_{tt} = c^2 u_{xx}$ ), heat equation ( $u_t = k u_{xx}$ ), convection-diffusion equation ( $u_t + c u_x = k u_{xx}$ ), to name just a few. It however turns out that the output of the standard-PINN is indeed nearly equal to the trivial solution at the point of initialization. Hence, convergence to the true solution during subsequent training becomes highly sensitive to the choice of  $\lambda$ s in (2), such that deviations from the trivial solution can be counterbalanced by improvements in (2d) and (2e). Even upon careful selection of  $\lambda$ s, the PINN’s output may still remain trapped at the flat function at regions far from the boundary and initial conditions (as seen in Figure 1b), since the physics loss is deceptively minimized in those regions.

## 2) Behavior of Standard Finite-Sized PINNs

In practice, the number of layers and nodes in a PINN are many but finite (unlike the asymptotic assumption of *Proposition 1*). Nonetheless, the initial solution is still *almost flat everywhere*; as indicated in Figure 1b. This can be understood by visualizing the “tanh” activation function which has slope close to 0 almost everywhere, except in regions close to the origin (where slope reaches 1). To gain further insight, we analyze the behavior of a single layer PINN with  $n$  neurons, “tanh” activation and scalar input  $x$ . The output can be written as  $\hat{u} = \sum_{i=1}^n w'_i \tanh(w_i x)$ , where  $w$  and  $w'$  are i.i.d.

$\mathcal{N}(0, 2/(n+1))$  under Xavier initialization. The input gradient:

$$\nabla_x \hat{u} = \sum_{i=1}^n w'_i w_i \operatorname{sech}^2(w_i x), \quad (11)$$

has a zero mean  $E[\nabla_x \hat{u}] = 0$  and variance:

$$\begin{aligned} \operatorname{Var}(\nabla_x \hat{u}) &= n \operatorname{Var}(w') \operatorname{Var}(w \operatorname{sech}^2(wx)) = \\ \frac{2n}{n+1} \operatorname{Var}(w \operatorname{sech}^2(wx)) &= \frac{2n}{n+1} (\operatorname{Var}(w) E[\operatorname{sech}^4(wx)] + \\ \operatorname{Cov}(w^2, \operatorname{sech}^4(wx)) - E[w \operatorname{sech}^2(wx)]^2) < \\ \frac{2n}{n+1} \operatorname{Var}(w) E[\operatorname{sech}^4(wx)]. \end{aligned} \quad (12)$$

The last inequality holds because  $E[w \operatorname{sech}^2(wx)] = 0$  and  $\operatorname{Cov}(w^2, \operatorname{sech}^4(wx)) < 0$  (note  $\operatorname{sech}^4(wx)$  is a strictly decreasing function of  $|w|$ ). The term  $E[\operatorname{sech}^4(wx)]$  in (12) equals to 1 at the input origin ( $x = 0$ ), and approaches zero very quickly when  $x$  is moving away from the origin. Hence, the variance (and magnitude) of input gradient is bounded by the variance of  $w$ ’s at the first hidden layer, which is inversely proportional to the number of neurons in the first hidden layer. For example, a single layer PINN with just 20 hidden neurons has an initial input gradient variance smaller than 0.2 everywhere. The lack of variability in input gradients,  $\nabla_x \hat{u}(x; \mathbf{w}) \approx 0$ , at initialization for even small or medium-sized PINNs translates into output flatness, thus leading to training behavior similar to the asymptotic case.

## III. PINNS IN SINUSOIDAL SPACES

### A. Introducing Sinusoidal Features in PINNs

Let us consider the inputs  $\mathbf{v} = [x, t]^T$  for simplicity of exposition. We define one instance of the sinusoidal mappings that act on PINNs’ low dimensional spatial-temporal inputs:

$$\gamma(\mathbf{v}) = \sin(2\pi(\mathbf{W}\mathbf{v} + \mathbf{b})), \quad (13)$$

where  $\mathbf{W} \in \mathbb{R}^{m \times d}$  is a real matrix related to the frequency of sinusoidal features and  $\mathbf{b} \in \mathbb{R}^{m \times 1}$  is a real vector related to phase lag. Here,  $m$  is a pre-defined number of sinusoidal features, although it can also be optimized as a hyper-parameter, and  $d$  is the number of coordinate inputs. We can incorporate the sinusoidal mapping  $\gamma(\mathbf{v})$  into the first hidden layer of a PINN

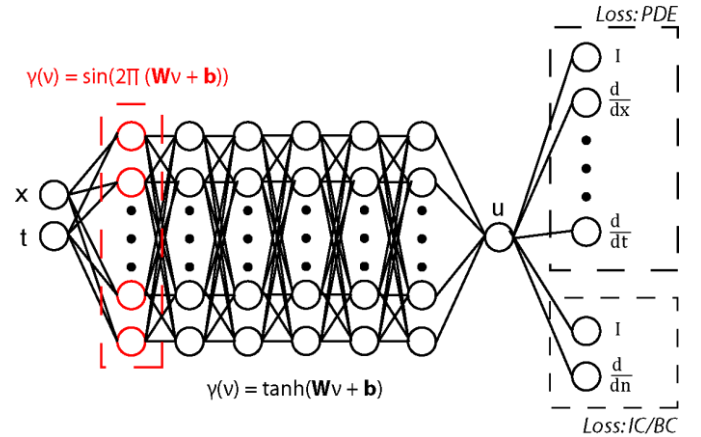


Fig. 2. The network architecture of the proposed sf-PINN.

by changing its activation function into  $\sin(2\pi\mathbf{z})$ , where  $\mathbf{z} = \mathbf{W}\mathbf{v} + \mathbf{b}$ . The weight and bias parameters of the first hidden layer now become the mapping parameters  $(\mathbf{W}, \mathbf{b})$ , and they can be optimized during the PINN training; see Figure 2. This PINN with sinusoidal features is referred to hereafter as *sf*-PINN.

For training of *sf*-PINNs, we propose to initialize the weights in  $\mathbf{W} \in \mathbb{R}^{m \times d}$  by sampling from the normal distribution  $\mathcal{N}(0, \sigma^2)$ , and the bias  $\mathbf{b} \in \mathbb{R}^{m \times 1}$  with a zero vector. This incurs an additional hyperparameter  $\sigma$  to tune, which we refer to hereafter as the *bandwidth* parameter; it has an immediate impact on the initial variability of the *sf*-PINN’s input gradients and is associated with the frequency range of the sinusoidal features. By adjusting the bandwidth, we can modulate the initial variability of *sf*-PINN to better match the frequency characteristic of the problem at hand. In practice, if the output frequency is unknown, the bandwidth needs to be selected by a grid search. Nevertheless, we found that bandwidth  $\sigma = 1$  is a practical default, and that the search range can be restricted between  $1e^{-1}$  and  $1e^1$  for most problems we have encountered. It may also be possible to infer potential bandwidth parameters based on fundamental frequencies of the physical system.

### B. Motivations behind Sinusoidal Spaces

We envision two key advantages of utilizing sinusoidal features in PINNs. These are discussed below.

#### 1) Circumventing the Trivial Local Minimum Trap

*sf*-PINNs also fall into the ambit of *Proposition 1* in the asymptotic case, since  $\|\sin(x) - \sin(x')\|_2^2 < \|x - x'\|_2^2, \forall x \neq x'$ . However, the distinguishing facet of *sf*-PINNs is that they allow to effectively elevate the variability of input gradients for small or medium-sized networks, thus avoiding being trapped in a trivial local minimum. Furthermore, the initial variability can be adjusted to match high-frequency patterns in the problem at hand. This is done by increasing the variance of  $w$ ’s at the sinusoidal mapping layer (i.e.,  $\sigma^2$  where  $\sigma$  is the *bandwidth* parameter) during initialization, as illustrated in Figure 3a. We do not induce additional variance for  $w$ ’s in the subsequent hidden layers to avoid changing backpropagation gradients’ distribution.

To elucidate the difference in input gradients’ variability between a small or medium-sized *sf*-PINN and *standard*-PINN, we consider a single layer PINN with  $n$  neurons, “sine” activation and scalar input  $x$ . Its input gradient:

$$\nabla_x \hat{u} = \sum_{i=1}^n w'_i w_i \cos(w_i x), \quad (14)$$

has a zero mean  $E[\nabla_x \hat{u}] = 0$  and variance:

$$\begin{aligned} \text{Var}(\nabla_x \hat{u}) &= n \text{Var}(w') \text{Var}(w \cos(wx)) = \\ &= \frac{2n}{n+1} (\text{Var}(w) E[\cos^2(wx)] + \text{Cov}(w^2, \cos^2(wx))) = \\ &= \frac{2n}{n+1} \left( \sigma^2 \left( \frac{1}{2} + \frac{1}{2} e^{-2x^2\sigma^2} \right) + \text{Cov}(w^2, \cos^2(wx)) \right). \end{aligned} \quad (15)$$

The  $\text{Cov}(w^2, \cos^2(wx))$  in (15) is negative near the input origin ( $x \approx 0$ ), but it quickly stabilizes at zero because of the periodic

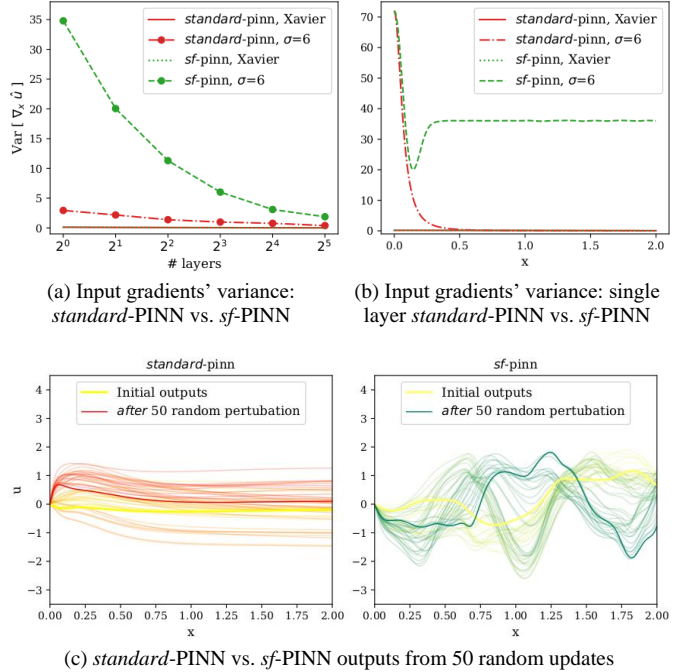


Fig. 3. (a) The averaged variance of input gradients along input  $x \in [0,2]$ , against the depth of *standard*- / *sf*-PINNs. The input gradients’ variance in a small or medium-sized *sf*-PINNs can be effectively elevated, by initializing the  $w$ ’s at the first (sinusoidal) hidden layer with a higher variance  $\sigma^2$ . The statistics are estimated from 5k independent initializations. (b) The profile of estimated input gradients’ variance from a single layer *standard*- / *sf*-PINN along input  $x \in [0,2]$ , under Xavier initialization and uplifted  $\sigma^2$  (squared of bandwidth). (c) Example outputs of a *standard*- / *sf*-PINN at initialization (bandwidth  $\sigma = 6$ ), and after 50 steps of random perturbations,  $\varepsilon \sim \mathcal{N}(0, 0.05^2)$  to their network parameters (lines with color transit from yellow to red and green, respectively). Apart from changing first hidden layer activation into sinusoidal mapping, both PINNs use identical architecture and initialization distribution.

nature of  $\cos(\cdot)$ . The term  $\frac{1}{2} e^{-2x^2\sigma^2}$  in (15) also approaches zero quickly when either  $\sigma$  or  $x$  is large. As a result, the *sf*-PINNs (even without the factor  $2\pi$  in mapping (13)) maintain a uniform input gradient variance,  $\text{Var}(\nabla_x \hat{u}) \approx \sigma^2$ , across the entire input domain, such that *the output is fluctuating everywhere*. The level of variability is effectively controlled by  $\sigma$ . This uniform variance in input gradients is preserved even if the *sf*-PINNs use standard monotonic activation such as “tanh” in subsequent hidden layers, albeit the scale of variability is reduced. On the contrary, *standard*-PINNs only receive a boost in variability at the region very near to the input origin if we increase  $\sigma$ , according to (12). The contrast is illustrated in Figure 3b.

It is reasonable to assume such difference in the input gradient properties (and therefore the output behavior) between a *standard*-PINN and a *sf*-PINN remains even after initialization. Figure 3c compares an example output from a *standard*-PINN and a *sf*-PINN with identical architecture and initialization distribution. We applied small random perturbations to their entire network parameters for 50 consecutive steps, mimicking a random walk. While the new solutions from the *standard*-PINN remain mostly flat, the perturbed *sf*-PINN generates a rich variety of fluctuating patterns on 1D input domain. This could help a *sf*-PINN to circumvent local minima in the PINN loss during training, since

it is less likely to be trapped in a trivial solution to the differential equation.

The successful learning of PINN is essentially predicated on matching the input gradients with the differential equation (1) in the entire domain. The *standard*-PINN may be suitable for problems with normally distributed inputs (i.e., samples are dense near the origin of input), but the input gradients' uniform variability in *sf*-PINNs suggests greater suitability for uniformly distributed inputs, which is the case for PINN problems.

## 2) Embedding Physically Relevant Structures into PINNs

Sinusoidal patterns occur naturally in numerous physical processes, for example, in analytical descriptions of wave propagation and solutions to the heat equation. For such problems, the sinusoidal features provide *sf*-PINNs an informed guess to the target solution, and potentially transform the loss landscape into an easier one to optimize. Given the same network initialization distribution, a *sf*-PINN may more easily find the desired sinusoidal patterns (input gradients profile) that match the inherent physical characteristics of the target solution, thus achieving significant speedup in training over a *standard*-PINN. It's worth noting that sinusoidal features do not necessarily constrain the output to be periodic.

### C. Empirical Observation in 1D Multi-Frequency ODE Problem

Because of the above reasons, *sf*-PINN has the potential to circumvent local minima in PINN loss and converge to the accurate solution much quicker. As an example, we train *sf*-PINN model to solve for the differential equation (3), and compare its training behavior against the *standard*-PINN and *standard*-DNN. The benefits are evident in Figure 1c. Good *sf*-PINN solutions are obtained within a much smaller number of optimization steps, for all 10 independent runs. Among the 3 models, the *sf*-PINN achieves the lowest mean squared error (MSE) against the ground truth solution by learning from the physics loss.

### D. Variants of Sinusoidal Features PINNs

In this section, we contextualize novel variations of sinusoidal mappings, including notable examples from the literature that we can describe using our *sf*-PINN framework.

#### 1) Cosinusoidal Features PINNs (*cf*-PINNs)

The sinusoidal mapping (13) can be changed from “sine” to “cosine”. A cosine function is equivalent to a sinusoidal function with a constant phase shift. The difference is that the *cf*-PINNs induce a strong bias towards a symmetric solution with respect to the origin when initialized with  $\mathbf{b} = \mathbf{0}$ , and its initial solution has a zero input gradient at the origin. Therefore, *cf*-PINNs may be preferred if the target solution is known to be symmetric around zero.

#### 2) Fourier Features PINNs (*ff*-PINNs)

The *ff*-PINNs replace (13) with pairs of “sine” and “cosine” (a constant phase shift of “sine”) mapping of the inputs, i.e.,

$$\gamma(\mathbf{v}) = [\sin(2\pi(\mathbf{W}\mathbf{v} + \mathbf{b})), \cos(2\pi(\mathbf{W}\mathbf{v} + \mathbf{b}))]^T. \quad (16)$$

Both “sine” and “cosine” components may share the same parameters ( $\mathbf{W}, \mathbf{b}$ ). It can be seen as combination of *sf*-PINNs and *cf*-PINNs.

#### 3) Random Fourier Features PINNs (*rf*-PINNs)

The *rf*-PINNs have the exact same setting as the *ff*-PINNs, except that the randomly initialized Fourier features (i.e., with both “sine” and “cosine” mappings) are not subsequently fine-tuned. The weights and bias parameters ( $\mathbf{W}, \mathbf{b}$ ) in the feature mapping layer of *rf*-PINNs are frozen during training. As suggested in recent studies [39, 40], Fourier mapping on inputs has a significant effect on the NTK's eigenvalue spectrum and convergence properties of the corresponding DNN/PINN.

#### 4) Sinusoidal Representation Network (SIRENs)

DNNs/PINNs with sinusoidal activation—SIRENS as per Sitzmann *et al.* [41]—can be seen as a specific implementation of *sf*-PINN with the “sine” activation adopted in *all hidden layers*. The introduction of sinusoidal activation in DNNs and association to Fourier neural network [42] can be dated back to the 1980s. They are regarded as difficult to train while not offering superior performance to other activations in common machine learning tasks [43], and are therefore uncommon in literature. However, some works in literature lately reported a superior performance with sinusoidal activations in PINNs [17, 44]. These studies however do not systematically explore the benefit of sinusoidal activation or elucidate why it performs better than other activation functions on PINN problems.

According to our analysis in Section III-B, we hypothesize that each of these variants of the sinusoidal mappings are functionally similar, and will have similar efficacy when applied to PINNs. In the following sections, we benchmark the performance of *sf*-PINNs and the above variants (except the *cf*-PINN) against *standard*-PINNs which use “tanh” activation in all hidden layers, across a wide range of forward and inverse modelling problems.

## IV. EXPERIMENT RESULTS ON FORWARD PROBLEM

We study the efficacy of *sf*-PINN and its variants as a mesh free method to solve differential equations, i.e., a forward problem. The PINN loss function (2) is defined by the residual terms from the differential equations over the entire computational domain, and the prescribed initial and boundary conditions. This loss is to be minimized such that the PINN output emulates the solution of the differential equation. The problem of solving differential equations is essentially transformed to a PINN learning problem. It is important to train a PINN towards its optimal loss value to avoid unphysical solutions.

The test problems include: 1D multi-frequency ODE, Helmholtz equation, Wave equation, Navier-Stokes (N-S) equation, Korteweg-de Vries (KdV) equation, and Burgers' equation. For each problem, we train different PINN models under a consistent setting. Then, we compute their MSE against the ground truth solution over a dense set of test points which are sampled from the problem domain. We run a series of experiments with different bandwidth parameter  $\sigma \in [1e^{-1}, 1e^1]$  and compare the MSE given by different PINNs.

TABLE I: PINN SETTINGS FOR TEST PROBLEMS

Problem	(a) 1D multi-frequency ODE	(b) 2D Helmholtz eqn.	(c) 1D transient wave eqn.	(d) 2D transient N-S eqns. (Taylor-Green vortex)	(e) 1D transient KdV eqn.	(f) 1D transient Burgers' eqn.
PINN architecture	$(x)-\mathbf{64}-20-20-20-(\hat{u})$	$(x,y)-\mathbf{64}-20-20-20-(\hat{u})$	$(x,t)-\mathbf{64}-50-50-50-(\hat{u})$	$(x,y,t)-\mathbf{64}-50-50-50-50-50-50-50-(\hat{u}, \hat{v}, \hat{p})$	$(x,t)-\mathbf{64}-50-50-50-(\hat{u})$	$(x,t)-\mathbf{64}-20-20-20-(\hat{u})$
Test set (no. points)	10000	256x256	256x256	101x101x51	257x251	256x100
Training batch size (no. points sampled for 1 evaluation of $\mathcal{L}_{DE} + \mathcal{L}_{IC} + \mathcal{L}_{BC}$ loss)	$100 + 0 + 1$	$450 + 0 + 50$	$450 + 40 + 10$	$450 + 40 + 10$	$480 + 10 + 10$	$470 + 20 + 10$
Max. training step	100,000	100,000	200,000	100,000	100,000	100,000

(1) For the PINN architecture, the numbers in between input and output represent the number of nodes in hidden layers. For example,  $(x)-\mathbf{64}-20-20-20-(\hat{u})$  indicates a single input  $x$ , followed by 4 hidden layers with 64, 20, 20 and 20 nodes in each layer, and a single output  $\hat{u}$ . The number of neurons (sinusoidal features) in first hidden layer (sinusoidal mappings layer) is highlighted in bold.

(2) The initial learning rate for PINN optimization is set at  $5e^{-3}$ , with a learning plan to reduce it by half on plateauing, until a min. learning rate  $1e^{-6}$  is reached.

(3) For the inverse problems described in Section V, the training batch size is 50 + 450 no. points sampled for 1  $\mathcal{L}_{Data} + \mathcal{L}_{DE}$  evaluation.

We further compare their MSE for a consistent  $\sigma = \sigma_{fixed}$  and different relative weights  $\lambda \in [1e^0, 1e^6]$  in the loss function, i.e.,  $\mathcal{L} = 1/\lambda \mathcal{L}_{DE} + \mathcal{L}_{IC} + \mathcal{L}_{BC}$ . We uniformly sample 25 different  $\sigma$ s and 25 different  $\lambda$ s in log space.

The general settings are summarized in Table I. We use the state-of-the-art SGD optimizer—ADAM—to train the PINN models for a fixed number of iterations. The *standard*-PINNs

use “tanh” activation function in all hidden layers. The “tanh” activation function is also used for the second and subsequent hidden layers for the *sf*-PINN variants (except SIRENs). We use Xavier initialization (except for SIRENs, where He uniform initialization [45] is recommended for effective training) for the network weights other than the first hidden (feature mapping) layer, with the latter being initialized with a  $\mathcal{N}(0, \sigma^2)$ .

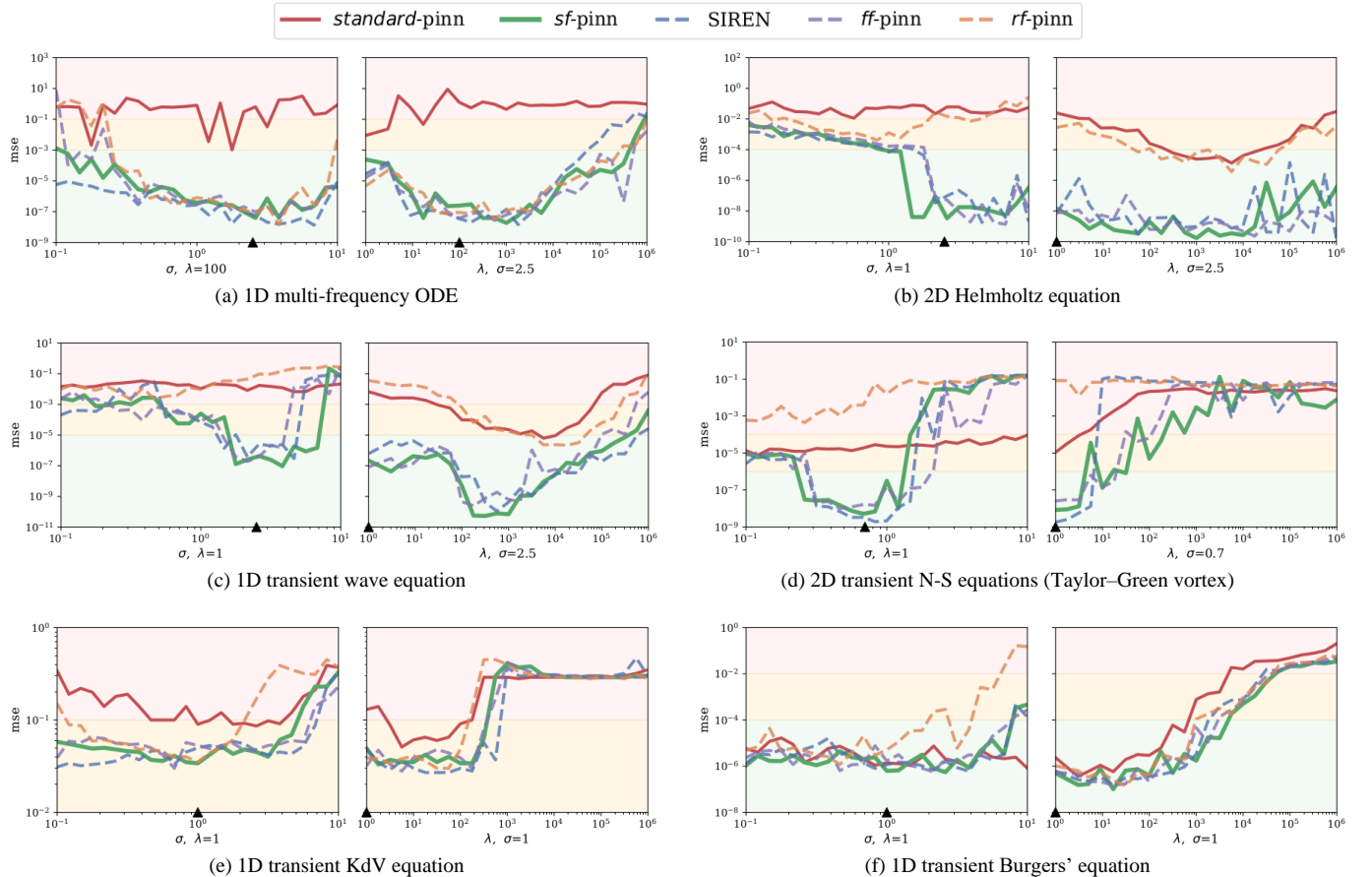


Fig. 4. The best MSE achieved by different PINNs over 5 independent runs, at  $\sigma \in [1e^{-1}, 1e^1]$ ,  $\lambda = \lambda_{fix}$  (left) and  $\lambda \in [1e^0, 1e^6]$ ,  $\sigma = \sigma_{fix}$  (right), for different test problems (a-f). The triangle symbol in  $\sigma$  plots indicates the  $\sigma$  value to be fixed for  $\lambda$  experiments, and vice versa. The background color provides a rough guide to the quality of PINNs, where those in the red region present a clear differentiation to the ground truth solution upon visual inspection. A fair solution can be found in yellow region, where some minor artifacts are still noticeable. The accurate solutions in green region are almost indistinguishable from the ground truth.

### A. Summary of Results

The best MSE achieved by different PINNs over 5 independent runs at various  $\sigma$  and  $\lambda$  values is compared in Figure 4. The empirical results reveal that the *sf*-PINN and its SIREN and *ff*-PINN variants give very similar performance. This confirms our hypothesis that the sinusoidal mapping of inputs (via the first hidden layer) is of utmost importance, whereas switching from “tanh” to “sine” activation function in the subsequent hidden layers (i.e., a SIREN) doesn’t affect the PINN results much. In addition, the full Fourier features mapping used by *ff*-PINN does not outperform the “sine” only mapping. However, we conclude there is a strong motivation to optimize the sinusoidal mapping over the use of random mapping, as evidenced by the fact that the MSE obtained from *rf*-PINN is consistently worse than other *sf*-PINN variants across almost all test problems.

Next, we compare the performance between *sf*-PINN and *standard*-PINN at different  $\sigma$  values. As expected, the change in  $\sigma$  does not critically affect the performance of *standard*-PINN, since the  $\sigma$  parameter does not significantly improve the total variability of initial input gradients. On the other hand, *sf*-PINN and its variants are  $\sigma$  dependent. Within an appropriate range of  $\sigma$ , *sf*-PINN dramatically improves in MSE by 3-4 orders of magnitude across several test problems. In addition, *sf*-PINN remains competitive as compared to *standard*-PINN for most of the  $\sigma$  range spanning  $[10^{-1}, 10^1]$ . The only exception is the 1D transient Burgers’ equation, where there is no significant improvement from using *sf*-PINN. Hence, the *standard*-PINN never out-performs the *sf*-PINN and its variants in our examples. In addition, the empirical results demonstrate that good *sf*-PINN models are attainable across a wider range of  $\lambda$ , as opposed to the *standard*-PINN.

### B. Individual Results for Forward Problems

In the following, we describe selected test problems and compare the solution obtained by *sf*-PINN and the *standard*-PINN (baseline).

#### 1) 1D Multi-Frequency ODE

This solution to the synthetic problem described in equation (3) is the summation of 3 sinusoids with different frequencies:

$$u(x) = \sin(hx) + a_1 \sin(a_2 hx) + b_1 \sin(b_2 hx), \quad (17)$$

where  $h=8$ ,  $a_1=1$ ,  $a_2=6$ ,  $b_1=1$ ,  $b_2=5$ . As shown in Figure 4a, the first set of results compare the *sf*-PINN (and its variants) against *standard*-PINN for different bandwidth parameter  $\sigma \in [10^{-1}, 10^1]$ , given the relative weight  $\lambda = 100$ . The second set of results compare their performance at various  $\lambda \in [10^0, 10^6]$ , given that  $\sigma = 2.5$ . Despite being a simple 1D problem, a *standard*-PINN faces difficulty in producing a solution with  $\text{MSE} < 10^{-3}$ . Moreover, changing  $\lambda$  in the loss function doesn’t help the *standard*-PINN to escape the bad local minimum on this test problem. On the other hand, the *sf*-PINN is significantly easier to train, in that an accurate solution can be obtained across a wide range of  $\sigma$  and  $\lambda$ . A larger  $\sigma$  is preferred to accommodate higher frequency components in the solution.

#### 2) 2D Helmholtz Equation (Multi-Frequency)

The Helmholtz equation is an important PDE in many physics and engineering systems such as optics, acoustics, electrostatics, and quantum mechanics. It has been used to demonstrate the PINN methodology in several prior studies. We first consider a Helmholtz equation of the following form:

$$u_{xx} + u_{yy} + u = q(x, y), \quad (18)$$

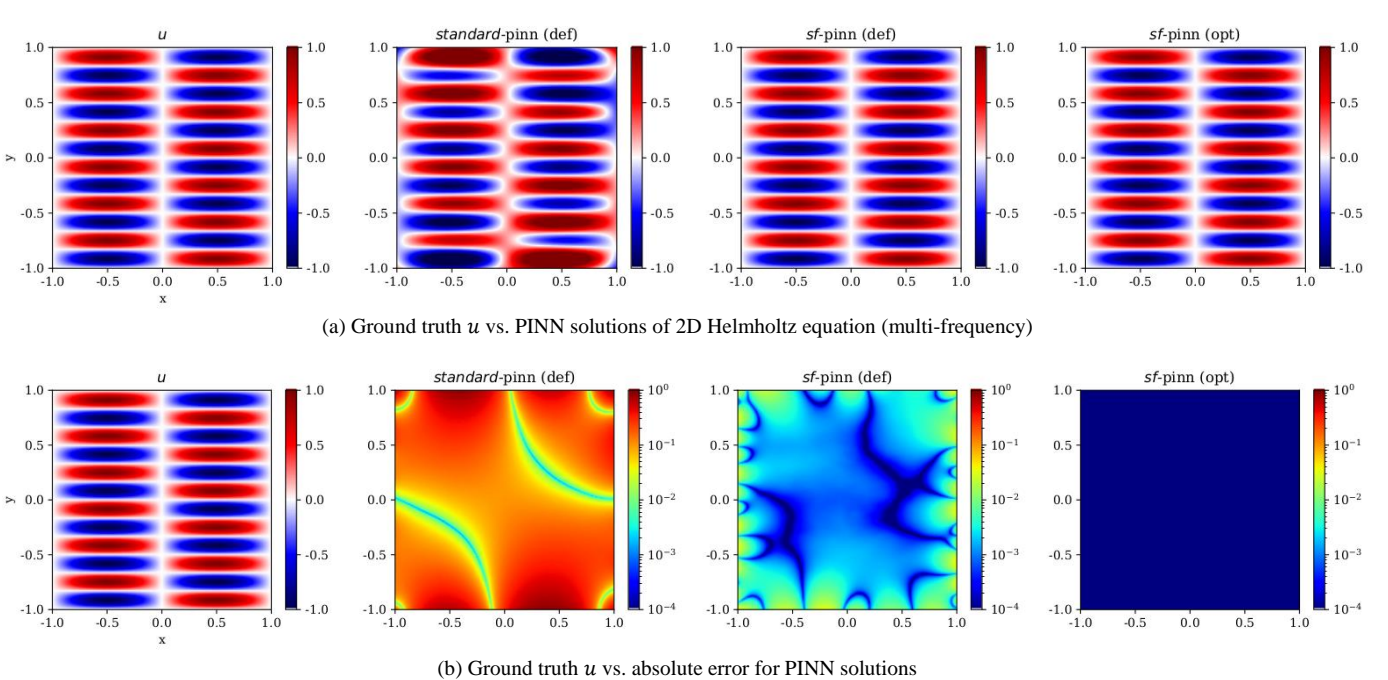


Fig. 5. (a) Comparison between the ground truth solution of 2D Helmholtz equation (multi-frequency) test problem and the solutions solved by a *standard*-PINN using default setting  $\sigma = 1, \lambda = 1$  (def), a *sf*-PINN using default setting  $\sigma = 1, \lambda = 1$  (def), and a *sf*-PINN using optimized setting  $\sigma = 2.5, \lambda = 1000$  (opt). (b) The absolute errors between ground truth and PINN solutions. Results are aggregated from 5 independent runs.

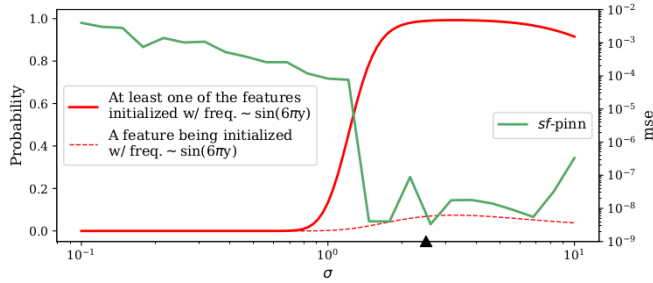


Fig. 6. The probability of having a sinusoidal feature (dashed red line) and at least one of the 64 sinusoidal features (solid red line) initialized with a frequency close to  $\sin(6\pi y)$ , versus initial bandwidth  $\sigma$ . The MSE of sf-PINN against ground truth versus  $\sigma$  is also overlaid in the same plot.

where the source term is defined as:

$$q(x, y) = (1 - \pi^2 - (6\pi)^2) \sin(\pi x) \sin(6\pi y). \quad (18b)$$

The equation (18) is solved by PINNs within the input domain  $x \in [-1, 1], y \in [-1, 1]$  with a Dirichlet boundary condition at the 4 domain boundaries. Its solution is the multiplication of 2 sinusoids with different frequency:

$$u(x, y) = \sin(\pi x) \sin(6\pi y). \quad (19)$$

A *standard*-PINN fails to properly solve the problem at default weight  $\lambda = 1$  (Figure 4b). As an example, the contour plots in Figure 5 compares the ground truth  $u$  and the averaged solution from 5 independent runs of a *standard*-PINN with default  $\sigma = 1, \lambda = 1$ . Obvious artifacts can be observed in the solution. A sf-PINN with the same default setting greatly improves the MSE by 3 orders of magnitude, i.e., from  $5.6e^{-2}$  to  $2.4e^{-5}$ . An even better sf-PINN model can be obtained by increasing  $\sigma$  to accommodate higher frequencies, for example setting  $\sigma = 2.5$

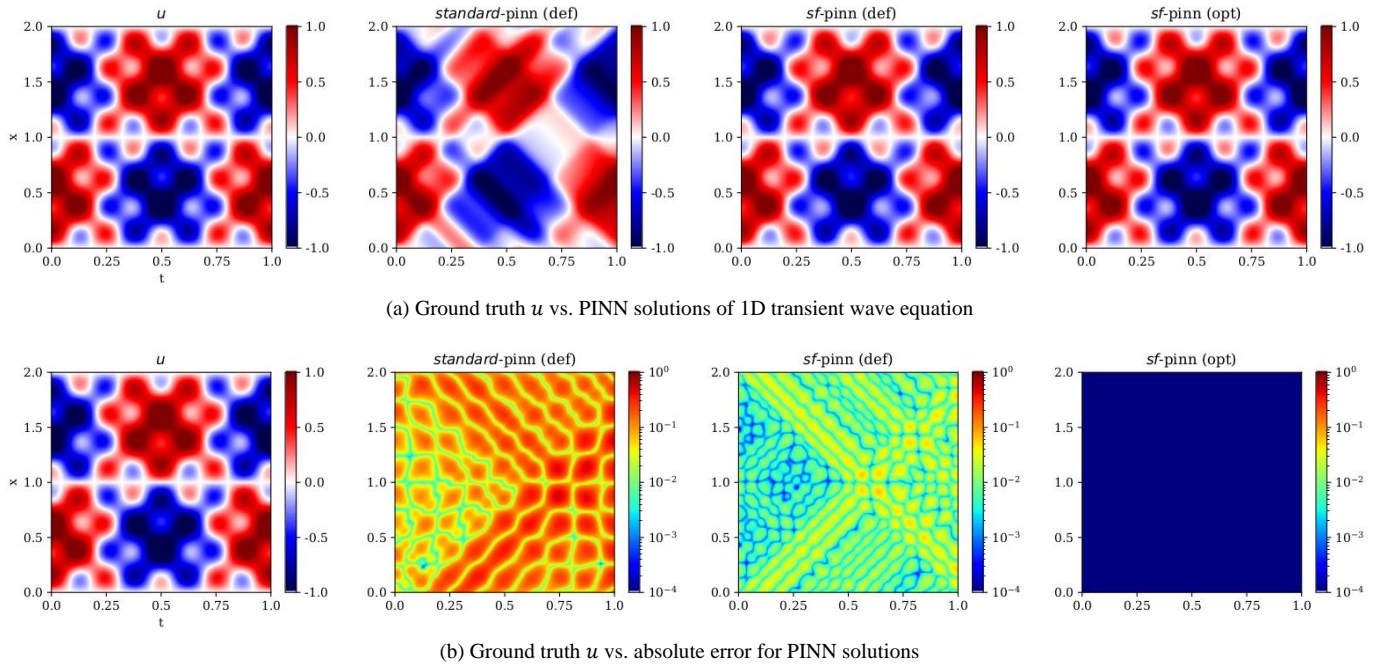


Fig. 7. (a) Comparison between the ground truth solution of 1D transient wave equation test problem and the solutions solved by a *standard*-PINN using default setting  $\sigma = 1, \lambda = 1$  (def), a sf-PINN using default setting  $\sigma = 1, \lambda = 1$  (def), and a sf-PINN using optimized setting  $\sigma = 2.5, \lambda = 180$  (opt). (b) The absolute errors between ground truth and PINN solutions. Results are aggregated from 5 independent runs.

leads to a very accurate solution. Among all sf-PINN models, the optimal  $\sigma$  and  $\lambda$  configuration achieves a MSE of  $1.1e^{-10}$ . This optimal sf-PINN solution is indistinguishable from the ground truth, with absolute error less than  $1e^{-4}$  almost everywhere within the domain (Figure 5).

The accuracy of sf-PINN model is significantly improved when the bandwidth  $\sigma$  is chosen to be greater than 1 for this problem. We show that it is possible to infer a suitable bandwidth parameter from the fundamental frequencies of the problem (if known) without running a grid search. We note that this test problem has a frequency of  $\sin(6\pi y)$ . We then compute the chance for a sinusoidal feature to be initialized with a frequency close to  $\sin(6\pi y)$ , e.g., between  $\sin(6\pi y)$  and  $\sin(7\pi y)$ . The probability trends are visualized in Figure 6. Given that there are 64 sinusoidal features in the sf-PINN model, the probability of having at least 1 of the sinusoidal features initialized with a frequency close to  $\sin(6\pi y)$  increases sharply when  $\sigma$  is chosen between 1 and 6. The sf-PINN model within this region is more easily trained, hence leading to more accurate solutions. On the other hand, if the  $\sigma$  is chosen to be too big, e.g., close to 10, the probability to sample a sinusoidal feature near the  $\sin(6\pi y)$  frequency starts decreasing. Then, the sf-PINN training may not be equally effective.

### 3) 1D Transient Wave Equation

The wave equation describes the wave phenomena arising in the physical world such as water waves, sound waves and seismic waves or light waves. We consider the wave equation in 1D:

$$u_{tt} = c^2 u_{xx}, \quad (20)$$

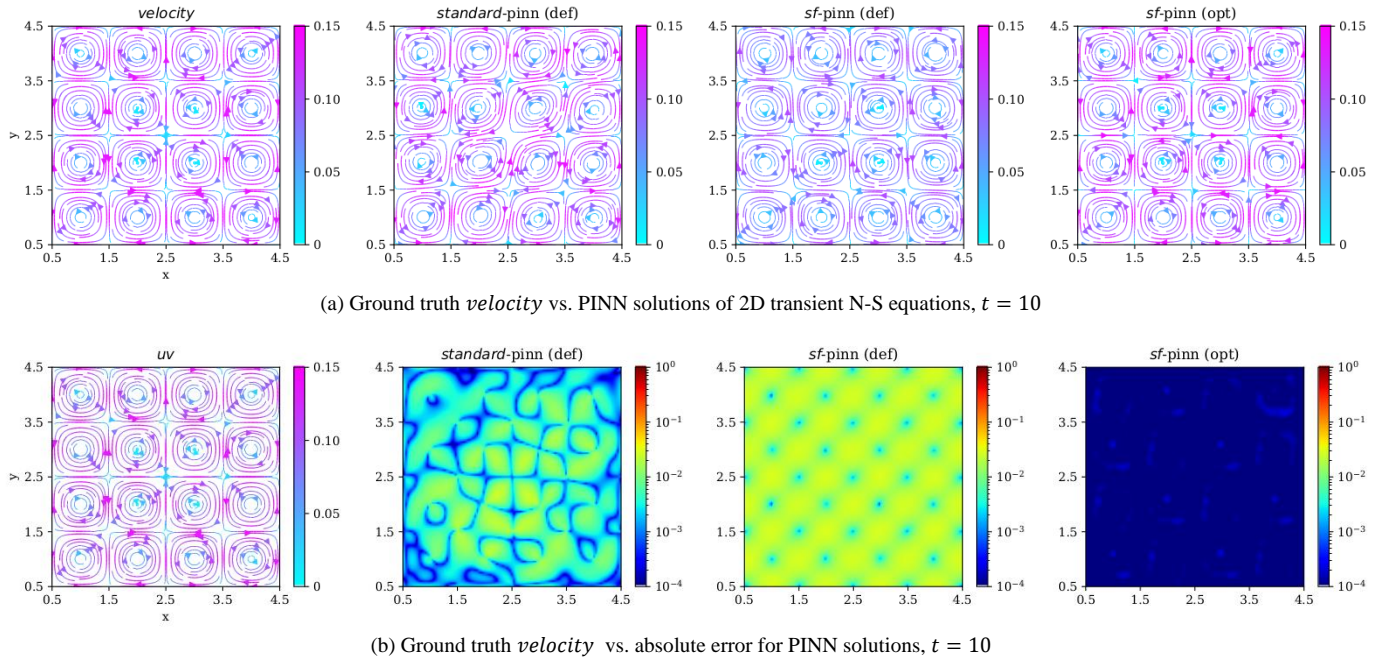


Fig. 8. (a) Comparison between the ground truth solution of 2D transient N-S equations test problem (at  $t = 10$ ) and the solutions solved by a *standard*-PINN using default setting  $\sigma = 1, \lambda = 1$  (def), a *sf*-PINN using default setting  $\sigma = 1, \lambda = 1$  (def), and a *sf*-PINN using optimized setting  $\sigma = 0.68, \lambda = 1$  (opt). The vortices are represented by streamlines, and the velocity magnitude is indicated by the color. (b) The absolute errors between ground truth and PINN solutions. Results are aggregated from 5 independent runs.

where  $c$  is a coefficient representing the velocity of the wave. We apply PINNs to solve equation (20) with the following initial and boundary conditions,

$$u(x, 0) = \sin(\pi x) + 0.5 \sin(4\pi x), \quad (20b)$$

$$u_t(x, 0) = 0, \quad (20c)$$

$$u(x_L, t) = u(x_U, t) = 0, \quad (20d)$$

where  $x_L = 0, x_U = 2$ . The spatial-temporal domain is  $x \in [0, 2], t \in [0, 1]$ . The above scenario leads to an oscillatory solution,

$$u(x, t) = \sin(\pi x) \cos(c\pi t) + 0.5 \sin(4\pi x) \cos(4c\pi t). \quad (21)$$

We set the coefficient  $c = 2$  for the test problem. As shown in Figure 4c, a *standard*-PINN using default relative weight  $\lambda = 1$  gives poor results. The solution from a *standard*-PINN using  $\sigma = 1, \lambda = 1$  is plotted in Figure 7. The contour plot shows a significant deviation from the ground truth ( $MSE=2e^{-2}$ ). The multi-frequency waves are not resolved correctly. On the other hand, a fairly accurate solution ( $MSE=2.6e^{-4}$ ) can be obtained by using a *sf*-PINN of the same setting. The accuracy of the *sf*-PINN solution greatly improves ( $MSE<1e^{-10}$ ) when an optimized  $\sigma$  and  $\lambda$  configuration is found.

#### 4) 2D Transient Navier–Stokes Equations (Taylor–Green vortex)

The N-S equations are a set of partial differential equations which describe the motion of viscous fluid—which determines the physics of many phenomena of scientific and engineering interest. In particular, the Taylor–Green vortex is an unsteady flow of decaying vortices described by 2D, incompressible N-S equations, which has exact closed form solution. Therefore,

it serves as a popular benchmark for testing and validation of numerical methods for solving incompressible N-S equations. The 2D incompressible N-S equations are given by:

$$u_x + v_y = 0, \quad (22)$$

$$u_t + u u_x + v u_y = -\frac{1}{\rho} p_x + v (u_{xx} + u_{yy}), \quad (22b)$$

$$v_t + u v_x + v v_y = -\frac{1}{\rho} p_y + v (v_{xx} + v_{yy}), \quad (22c)$$

where  $u, v$  are the flow velocity,  $p$  is the pressure,  $\rho$  is the density and  $v$  is the kinematic viscosity of the fluid. The first of the above equation represents the continuity equation and the other two represent the momentum equations. The  $u, v, p$  solutions of Taylor–Green vortex problem are given by,

$$u(x, y, t) = -\cos(\pi x) \sin(\pi y) \exp(-2\pi^2 vt), \quad (23a)$$

$$v(x, y, t) = \sin(\pi x) \cos(\pi y) \exp(-2\pi^2 vt), \quad (23b)$$

$$p(x, y, t) = -\frac{\rho}{4} [\cos(2\pi x) + \cos(2\pi y)] \exp(-4\pi^2 vt). \quad (23b)$$

The problem is solved by using  $u(x, y, 0), v(x, y, 0), p(x, y, 0)$  as the initial condition. At the 4 spatial domain boundaries, a Dirichlet boundary condition is specified for  $u, v$ , in addition to a Neumann boundary condition for  $p$ . The problem is solved within the spatial-temporal domain  $x \in [0.5, 4.5], y \in [0.5, 4.5], t \in [0, 10]$  with  $\rho = 1, v = 0.01$ .

The PINN results at various  $\sigma$  and  $\lambda$  values are shown in Figure 4d. In this test problem, the MSE is computed for the Euclidean norm of 2D velocity vector between ground truth and PINN solution. Although the *standard*-PINN could achieve a solution with  $MSE \sim 1e^{-5}$ , the flow visualization (Figure 8) of velocity streamlines at the final time step reveals that the

vortices in the center have been diverted and their shapes are distorted. On the other hand, the vortices are well maintained in the solution given by a *sf*-PINN using the same default setting. With an appropriately chosen  $\sigma$ , e.g.  $\sigma = 0.68$ , the MSE of a *sf*-PINN solution drops significantly to  $\sim 10^{-9}$ . As shown in Figure 8, the pattern and magnitude of the vortices are almost indistinguishable from the ground truth.

(The detailed results for the remaining test problems, i.e., 1D transient KdV and Burgers' equations, are omitted).

## V. EXPERIMENT RESULTS ON INVERSE PROBLEM

In an inverse problem, the outcome of differential equation is available or partially available in the form of data. The objective is to infer certain unknowns in the formulation of the differential equation or initial and boundary conditions. These unknown variable(s) are optimized together with the PINN network parameters with respect to the data-constrained loss function (2). The PINN model infers an estimated value for the variable, as well as the solution over the problem domain.

To investigate the effectiveness of *sf*-PINN for inverse

problem, we carried out experiments on the wave equation and N-S equations. We consider the scenario where the governing equation of the dynamical system is known but some system property is unknown, i.e., there is 1 unknown variable in the differential equation. Given the observation data, the task is to infer the unknown wave velocity  $c$  in the wave equation (20), and the kinematic viscosity  $\nu$  in the N-S equations (22). The exact initial and boundary conditions are also unknown, besides what is observed from the data. Our PINN loss function for inverse problem takes the form  $\mathcal{L} = \mathcal{L}_{Data} + 1/\lambda \mathcal{L}_{DE}$ . It is important to note that the collocation points for computing the  $\mathcal{L}_{DE}$  can be arbitrarily sampled within the problem domain, independent of the observed data.

For each test problem, we further consider a scenario whereby the observation data is dense, and a scenario whereby the observation data is sparse. In each of the scenarios, we run a series of experiments with different bandwidth parameter  $\sigma \in [10^{-1}, 10^1]$  and compare the MSE of the approximated solution given by *sf*-PINN, SIRENS and *standard*-PINN. The PINN model and training settings are almost identical to the forward problem (TABLE I).

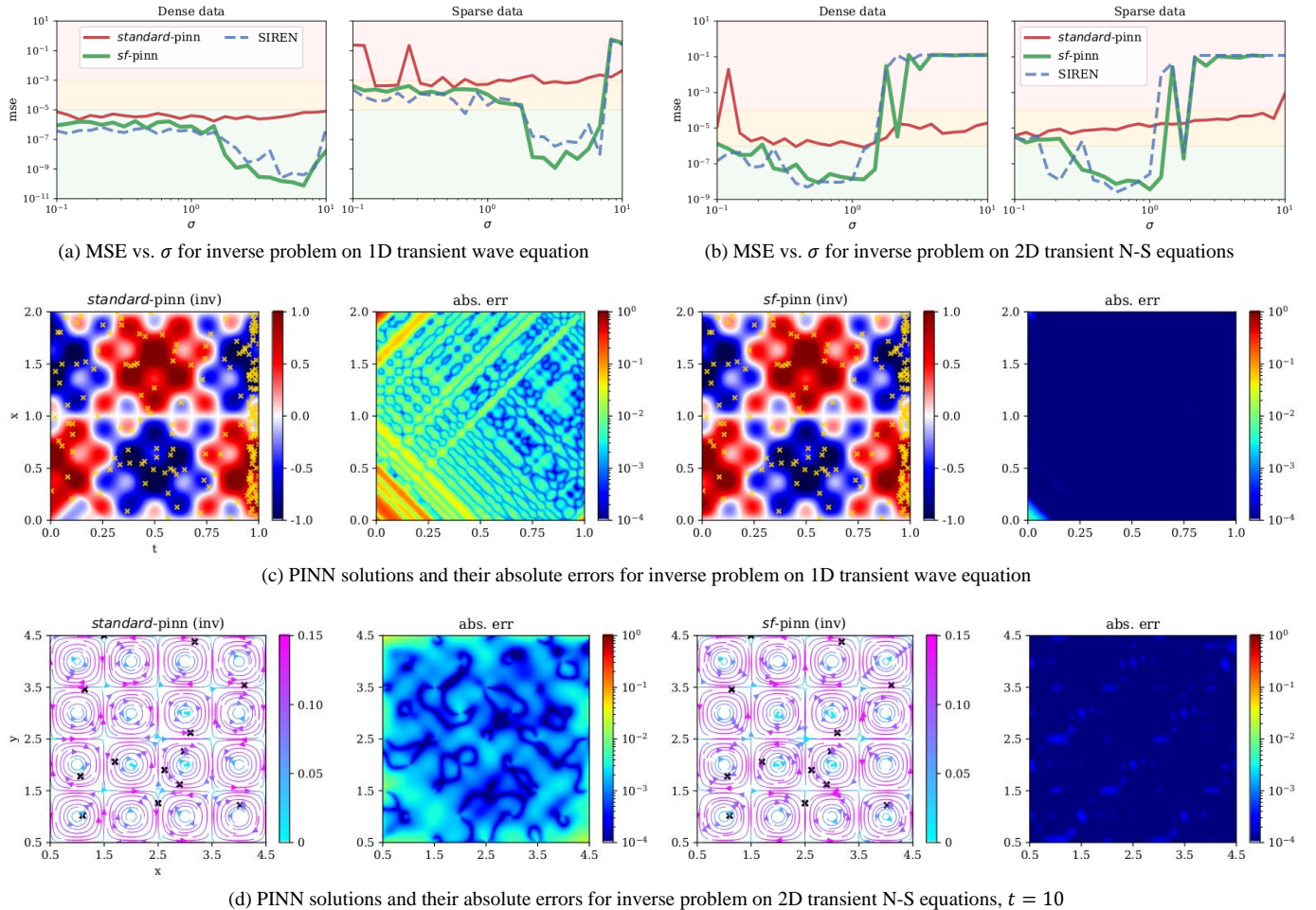


Fig. 9. The best MSE achieved by different PINNs over 5 independent runs at  $\sigma \in [10^{-1}, 10^1]$ , for inverse problem on (a) 1D transient wave equation and (b) 2D transient N-S equations, given that the data are densely observed (left) or only sparsely observed (right). The  $\lambda = 180$  for wave equation and  $\lambda = 1$  for N-S equations are chosen based on prior experiments for the forward problem. (c) The solutions to wave equation inverse problem solved by a *standard*-PINN ( $\sigma = 1, \lambda = 180$ ) and a *sf*-PINN ( $\sigma = 2.6, \lambda = 180$ ) given sparse data (highlighted in gold-x), and their absolute errors against the ground truth. (d) The solutions to N-S equations inverse problem solved by a *standard*-PINN ( $\sigma = 1, \lambda = 1$ ) and a *sf*-PINN ( $\sigma = 0.83, \lambda = 1$ ) given sparse data (highlighted in black-x), and their absolute errors against the ground truth. Results in (c-d) are aggregated from 5 independent runs.

### A. Individual Results for Inverse Problems

#### 1) 1D Transient Wave Equation

In Figure 9a, the best MSE achieved by different PINNs over 5 independent runs at various  $\sigma$  values are compared. The empirical results reveal that the *sf*-PINN and its SIREN variant give very similar performance, and they outperform *standard*-PINN in both dense ( $n = 256 \times 256$ ) and sparse ( $n = 200$ , with greater concentration at later time) data scenarios. The *sf*-PINN is particularly beneficial in sparse data scenario. The lack of data increases the difficulty of PINN training, hindering a *standard*-PINN from obtaining an accurate solution. The solution from a *standard*-PINN using  $\sigma = 1, \lambda = 180$  and its absolute error (MSE=6e<sup>-4</sup>) against the ground truth are plotted in Figure 9c. The mean of estimated values for the unknown  $c$  in the wave equation is 1.999 (sd = 1.7e<sup>-3</sup>), out of 5 independent runs. On the other hand, a very accurate solution (MSE=3.2e<sup>-8</sup>) can be obtained by using a *sf*-PINN with an appropriately chosen bandwidth ( $\sigma = 2.6, \lambda = 180$ ). The model also accurately infers the unknown  $c$  as 2 (sd = 7.3e<sup>-6</sup>). The results suggest that the *sf*-PINN can more accurately infer the dynamical behavior backward in time based on sparsely available historical data and the currently observed information, without knowing the complete physics, in addition to more accurately inferring the unknown system parameter  $c$ .

#### 2) 2D Transient Navier–Stokes Equations (Taylor–Green Vortex)

The best MSE achieved by different PINNs over 5 independent runs at various  $\sigma$  values are plotted in Figure 9b. The results demonstrate the *sf*-PINN’s superior ability to infer the correct solution from an inverse problem involving the N-S equations. They achieve similar accuracy for both dense ( $n = 101 \times 101 \times 51$ ) and sparse ( $n = 600$ ) data scenarios, with an appropriately chosen bandwidth. Figure 9d visualizes the velocity streamlines at the final timestamp, and the absolute error of the solutions obtained by a *standard*-PINN ( $\sigma = 1, \lambda = 1$ ) and a *sf*-PINN ( $\sigma = 0.83, \lambda = 1$ ). Their MSE against the ground truth are 1.4e<sup>-5</sup> vs. 6.9e<sup>-9</sup> respectively. The results are inferred from a set of sparse samples which are randomly distributed over the 3D spatial-temporal domain. The ground truth is  $v = 1e^{-2}$  in the N-S equations. Both *standard*-PINN and *sf*-PINN are able to accurately infer the unknown  $v$  in the N-S equations, with estimates of 9.97e<sup>-3</sup> (sd = 3.1e<sup>-5</sup>) and 9.998e<sup>-3</sup> (sd = 2.4e<sup>-6</sup>) respectively.

## VI. CONCLUSIONS

This paper analyzes and provides theoretical reasons for why standard PINNs frequently exhibit training difficulty. In particular, we observed significant issues even on a relatively straightforward 1D ODE model problem. We hypothesized this issue originates from the limited variability in input gradients of a standard PINN, resulting in the tendency towards being trapped in deceptive local optimum (that minimizes residual terms) right at the onset of PINN training, while still being far away from the true solution.

We then motivated the use of sinusoidal space with PINNs. In particular, we provided intuition for how such sinusoidal

mappings can overcome the trainability issues encountered by a standard PINN. We then demonstrated that these improvements are consistent across a whole range of forward and inverse modelling problems spanning multiple physics domains. In addition, we made the following observations for the use of *sf*-PINNs.

Firstly, while several works earlier demonstrated the superior performance of Fourier feature mapping relative to standard spatial-temporal inputs, we show in this work that the use of “sine” alone in PINNs can already yield many of the benefits from full Fourier features mapping. In particular, we believe it is not so much the use of Fourier features per se that yields the improvement, but the improved input gradient properties as outlined in Section III-B. Hence, the exact composition of the sinusoidal feature map in terms of whether they contain sinusoidal or cosinusoidal terms is less impactful than that they are incorporated in place of the “tanh” function in the first layer. Similarly, while some studies use sinusoidal activation function in all hidden layers, we present results here that suggest that the sinusoidal mapping of inputs in the first layer is most important, and we consistently observe that incorporation of a sinusoidal mapping in the first layer (*sf*-PINNs) alone can produce similar if not better performance.

Secondly, through extensive experimental studies, we demonstrate that fine-tuning of sinusoidal features can lead to significant improvement in modeling. While this can lead to extra effort in tuning the *sf*-PINNs, a properly tuned bandwidth can also reduce the need for sophisticated tuning of the loss composition required for *standard*-PINNs, as discussed in other work. This suggests that the use of *sf*-PINNs is an alternate route to addressing some of the PINN training challenges previously identified.

Lastly, while PINNs have shown tremendous potential thus far, it is important for future research to further improve the efficiency and efficacy of PINN training to unleash its full potential as a theory-guided AI model for broad science and engineering applications.

## REFERENCES

- [1] A. Karpatne, G. Atluri, J. H. Faghmous, M. Steinbach, A. Banerjee, A. Ganguly, S. Shekhar, N. Samatova, and V. Kumar, “Theory-guided data science: A new paradigm for scientific discovery from data,” *IEEE Transactions on Knowledge and Data Engineering*, vol. 29, no. 10, pp. 2318–2331, oct 2017.
- [2] G. E. Karniadakis, I. G. Kevrekidis, L. Lu, P. Perdikaris, S. Wang, and L. Yang, “Physics-informed machine learning,” *Nature Reviews Physics*, may 2021.
- [3] M. Raissi, P. Perdikaris, and G. Karniadakis, “Physics-informed neural networks: A deep learning framework for solving forward and inverse problems involving nonlinear partial differential equations,” *Journal of Computational Physics*, vol. 378, pp. 686–707, feb 2019.
- [4] M. Raissi, A. Yazdani, and G. E. Karniadakis, “Hidden fluid mechanics: Learning velocity and pressure fields from flow visualizations,” *Science*, vol. 367, no. 6481, pp. 1026–1030, jan 2020.
- [5] X. Jin, S. Cai, H. Li, and G. E. Karniadakis, “NSFnets (navier-stokes flow nets): Physics-informed neural networks for the incompressible navier-stokes equations,” *Journal of Computational Physics*, vol. 426, p. 109951, feb 2021.
- [6] S. Goswami, C. Anitescu, S. Chakraborty, and T. Rabczuk, “Transfer learning enhanced physics informed neural network for phase-field modeling

of fracture," *Theoretical and Applied Fracture Mechanics*, vol. 106, p. 102447, apr 2020.

[7] E. Haghigat, M. Raissi, A. Moure, H. Gomez, and R. Juanes, "A physics-informed deep learning framework for inversion and surrogate modeling in solid mechanics," *Computer Methods in Applied Mechanics and Engineering*, vol. 379, p. 113741, jun 2021.

[8] Y. Chen, L. Lu, G. E. Karniadakis, and L. D. Negro, "Physics-informed neural networks for inverse problems in nano-optics and metamaterials," *Optics Express*, vol. 28, no. 8, p. 11618, apr 2020.

[9] K. Shukla, P. C. D. Leoni, J. Blackshire, D. Sparkman, and G. E. Karniadakis, "Physics-informed neural network for ultrasound nondestructive quantification of surface breaking cracks," *Journal of Nondestructive Evaluation*, vol. 39, no. 3, aug 2020.

[10] J. Berg and K. Nyström, "A unified deep artificial neural network approach to partial differential equations in complex geometries," *Neurocomputing*, vol. 317, pp. 28–41, nov 2018.

[11] J. Sirignano and K. Spiliopoulos, "DGM: A deep learning algorithm for solving partial differential equations," *Journal of Computational Physics*, vol. 375, pp. 1339–1364, dec 2018.

[12] W. E and B. Yu, "The deep ritz method: A deep learning-based numerical algorithm for solving variational problems," *Communications in Mathematics and Statistics*, vol. 6, no. 1, pp. 1–12, feb 2018.

[13] K. Li, K. Tang, T. Wu, and Q. Liao, "D3m: A deep domain decomposition method for partial differential equations," *IEEE Access*, vol. 8, pp. 5283–5294, 2020.

[14] C. Michoski, M. Milosavljevic, T. Oliver, and D. R. Hatch, "Solving differential equations using deep neural networks," *Neurocomputing*, vol. 399, pp. 193–212, jul 2020.

[15] J. C. Wong, A. Gupta, and Y.-S. Ong, "Can transfer neuroevolution tractably solve your differential equations?" *IEEE Computational Intelligence Magazine*, vol. 16, no. 2, pp. 14–30, may 2021.

[16] M. Raissi, "Deep hidden physics models: Deep learning of nonlinear partial differential equations," *Journal of Machine Learning Research*, vol. 19, no. 25, pp. 1–24, 2018. [Online]. Available: <http://jmlr.org/papers/v19/18-046.html>

[17] M. Raissi, Z. Wang, M. S. Triantafyllou, and G. E. Karniadakis, "Deep learning of vortex-induced vibrations," *Journal of Fluid Mechanics*, vol. 861, pp. 119–137, dec 2018.

[18] G. Kissas, Y. Yang, E. Hwang, W. R. Witschey, J. A. Detre, and P. Perdikaris, "Machine learning in cardiovascular flows modeling: Predicting arterial blood pressure from non-invasive 4d flow MRI data using physics-informed neural networks," *Computer Methods in Applied Mechanics and Engineering*, vol. 358, p. 112623, jan 2020.

[19] A. Karpatne, W. Watkins, J. Read, and V. Kumar, "Physics-guided neural networks (pgnn): An application in lake temperature modeling."

[20] M. A. Nabian and H. Meidani, "Physics-driven regularization of deep neural networks for enhanced engineering design and analysis," *Journal of Computing and Information Science in Engineering*, vol. 20, no. 1, sep 2019.

[21] L. Sun, H. Gao, S. Pan, and J.-X. Wang, "Surrogate modeling for fluid flows based on physics-constrained deep learning without simulation data," *Computer Methods in Applied Mechanics and Engineering*, vol. 361, p. 112732, apr 2020.

[22] N. Wandel, M. Weinmann, and R. Klein, "Learning incompressible fluid dynamics from scratch - towards fast, differentiable fluid models that generalize," in *International Conference on Learning Representations (ICLR)*, 2021. [Online]. Available: <https://arxiv.org/abs/2006.08762>

[23] O. Fuks and H. A. Tchelepi, "Limitations of physics informed machine learning for nonlinear two-phase transport in porous media," *Journal of Machine Learning for Modeling and Computing*, vol. 1, no. 1, 2020.

[24] L. McClenney and U. Braga-Neto, "Self-adaptive physics-informed neural networks using a soft attention mechanism."

[25] D. P. Kingma and J. Ba, "Adam: A method for stochastic optimization," *arXiv preprint arXiv:1412.6980*, 2014.

[26] Y. Shin, "On the convergence of physics informed neural networks for linear second-order elliptic and parabolic type PDEs," *Communications in Computational Physics*, vol. 28, no. 5, pp. 2042–2074, jun 2020.

[27] S. Wang, X. Yu, and P. Perdikaris, "When and why pinns fail to train: A neural tangent kernel perspective."

[28] S. Wang, Y. Teng, and P. Perdikaris, "Understanding and mitigating gradient pathologies in physics-informed neural networks."

[29] M. Elhamod, J. Bu, C. Singh, M. Redell, A. Ghosh, V. Podolskiy, W.-C. Lee, and A. Karpatne, "Cophy-pgnn: Learning physics-guided neural networks with competing loss functions for solving eigenvalue problems."

[30] R. van der Meer, C. Oosterlee, and A. Borovykh, "Optimally weighted loss functions for solving pdes with neural networks."

[31] R. Pascanu, T. Mikolov, and Y. Bengio, "On the difficulty of training recurrent neural networks," in *ICML*, 2013.

[32] E. Haghigat and R. Juanes, "SciANN: A keras/TensorFlow wrapper for scientific computations and physics-informed deep learning using artificial neural networks," *Computer Methods in Applied Mechanics and Engineering*, vol. 373, p. 113552, jan 2021.

[33] O. Hennigh, S. Narasimhan, M. A. Nabian, A. Subramaniam, K. Tangsali, M. Rietmann, J. del Aguila Ferrandis, W. Byeon, Z. Fang, and S. Choudhry, "Nvidia simnet™: an ai-accelerated multi-physics simulation framework."

[34] L. Lu, X. Meng, Z. Mao, and G. E. Karniadakis, "DeepXDE: A deep learning library for solving differential equations," *SIAM Review*, vol. 63, no. 1, pp. 208–228, jan 2021.

[35] A. G. Baydin, B. A. Pearlmutter, A. A. Radul, and J. M. Siskind, "Automatic differentiation in machine learning: a survey," *Journal of Machine Learning Research*, vol. 18, no. 153, pp. 1–43, 2018. [Online]. Available: <http://jmlr.org/papers/v18/17-468.html>

[36] X. Glorot and Y. Bengio, "Understanding the difficulty of training feedforward neural networks," in *AISTATS*, 2010.

[37] Y. Bengio, "Practical recommendations for gradient-based training of deep architectures," in *Neural networks: Tricks of the trade*. Springer, 2012, pp. 437–478.

[38] N. Rahaman, A. Baratin, D. Arpit, F. Draxler, M. Lin, F. Hamprecht, Y. Bengio, and A. Courville, "On the spectral bias of neural networks," in *International Conference on Machine Learning*. PMLR, 2019, pp. 5301–5310.

[39] M. Tancik, P. P. Srinivasan, B. Mildenhall, S. Fridovich-Keil, N. Raghavan, U. Singhal, R. Ramamoorthi, J. T. Barron, and R. Ng, "Fourier features let networks learn high frequency functions in low dimensional domains."

[40] S. Wang, H. Wang, and P. Perdikaris, "On the eigenvector bias of fourier feature networks: From regression to solving multi-scale pdes with physics-informed neural networks."

[41] V. Sitzmann, J. N. Martel, A. W. Bergman, D. B. Lindell, and G. Wetzstein, "Implicit neural representations with periodic activation functions," in *Proc. NeurIPS*, 2020.

[42] A. Lapedes and R. Farber, "Nonlinear signal processing using neural networks: Prediction and system modelling," 1987.

[43] G. Parascandolo, H. Huttunen, and T. Virtanen, "Taming the waves: sine as activation function in deep neural networks," 2017.

[44] N. Zobeiry and K. D. Humfeld, "A physics-informed machine learning approach for solving heat transfer equation in advanced manufacturing and engineering applications," *Engineering Applications of Artificial Intelligence*, vol. 101, p. 104232, may 2021.

[45] K. He, X. Zhang, S. Ren, and J. Sun, "Delving deep into rectifiers: Surpassing human-level performance on imagenet classification," *2015 IEEE International Conference on Computer Vision (ICCV)*, pp. 1026–1034, 2015.